Inorganic Chemistry

Article

pubs.acs.org/IC

Making Oxidation Potentials Predictable: Coordination of Additives Applied to the Electronic Fine Tuning of an Iron(II) Complex

Stefan Haslinger,[†] Jens W. Kück,[†] Eva M. Hahn,[†] Mirza Cokoja,[†] Alexander Pöthig,[†] Jean-Marie Basset,[‡] and Fritz E. Kühn*[,†]

[†]Inorganic Chemistry/Molecular Catalysis, Catalysis Research Center, Technische Universität München (TUM), Ernst-Otto-Fischer-Straße 1, 85747 Garching bei München, Germany

[‡]Catalysis Center, King Abdullah University of Science and Technology (KAUST), Thuwal 23955-6900, Kingdom of Saudi Arabia

Supporting Information

ABSTRACT: This work examines the impact of axially coordinating additives on the electronic structure of a bioinspired octahedral low-spin iron(II) N-heterocyclic carbene (Fe-NHC) complex. Bearing two labile *trans*-acetonitrile ligands, the Fe-NHC complex, which is also an excellent oxidation catalyst, is prone to axial ligand exchange. Phosphine- and pyridine-based additives are used for substitution of the acetonitrile ligands. On the basis of the resulting defined complexes, predictability of the oxidation potentials is demonstrated, based on a correlation between cyclic voltammetry experiments and density functional theory calculated molecular orbital energies. Fundamental insights into changes of the electronic properties upon axial ligand exchange and the impact on related attributes will finally lead to target-oriented manipulation of the electronic properties and consequently to the effective tuning of the reactivity of bioinspired systems.

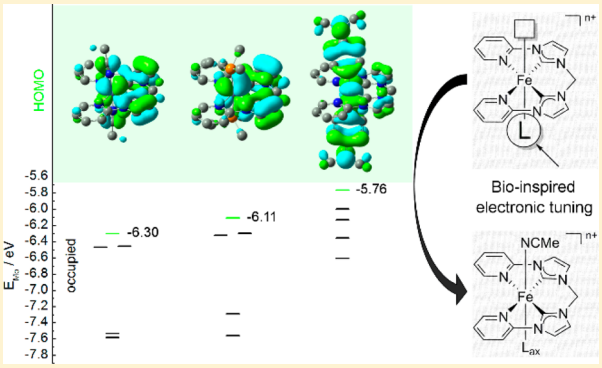

INTRODUCTION

Remarkable reactivity has been achieved with biologically inspired molecular systems in recent years.[1−9] Enzymes containing iron or copper active sites are used as blueprints for accessing these bioinspired and biomimetic systems.[1,10,11] Adapting design principles of metalloenzymes to synthetic catalysts may help to establish environmentally friendly processes, based on abundant and nontoxic metals and reagents.[1] A plethora of bioinspired catalytic applications is known, ranging from C−H bond oxidation to olefin epoxidation and asymmetric hydrogenation.[1,7,12−21] Apart from steric encumbrance, biological ligand spheres alter the electronic properties of the metal cofactor significantly. Therefore, artificial ligand systems that are easily accessible and tunable in terms of sterics and electronics allow for the adaption of biologically derived tools to synthetic catalysts. Consequently, a variety of artificial high-valent iron intermediates of bioinspired catalytic processes were isolated and studied thoroughly, stabilized by multidentate amine-, pyridine-, or N-heterocyclic carbene (NHC)-based ligands.[6,14,22−26] In cytochrome P450 (cyt-P450), the most extensively studied enzyme capable of dioxygen activation, the reactivity of the iron center is influenced to a considerable extent by coordination of an axial ligand. A push−pull effect induced by the apical thiolate enables O−O bond cleavage, which is widely accepted as the crucial step in the reactivity of dioxygen- and peroxide-based iron oxidation chemistry.[1,27,28] This effect inspired target-oriented manipulations in order to tune oxidation potentials and activation barriers for synthetic systems with specific applications.[29,30]

Recently, we expanded the field of Fe-NHC-catalyzed transformations by reporting the Fe^{II}-NCCN-ligated [NCCN = bis(pyridylimidazol-2-ylidene)methane] complex **1** (Figure 1) as an efficient epoxidation and hydroxylation catalyst.[31,32]

Complex **1** exhibits two labile *trans*-acetonitrile ligands and is therefore an excellent candidate for bioinspired axial ligand modification analogous to cyt-P450. Various axially coordinating neutral ligands are subject to detailed investigations. For several applications of transition-metal complexes, it is well

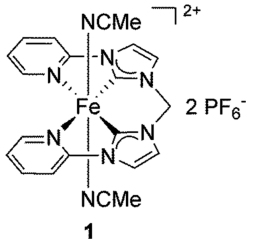

1

Figure 1. Structure of the Fe-NHC complex **1** bearing a tetradentate NCCN ligand and two *trans*-acetonitrile ligands.[31]

Received: July 10, 2014
Published: October 21, 2014

Table 1. Crystallographic Data for Fe-NHC Complexes 2 and 4−6 with Different Axial Ligands L_{ax}

	2 (L_{ax} = PMe_3)	4 (L_{ax} = DMAP)	5 (L_{ax} = py)	6 (L_{ax} = Me^inico)
formula	$C_{23}H_{32}F_{12}FeN_6P_4$	$C_{35}H_{40}F_{12}FeN_{12}P_2$	$C_{27}H_{24}F_{12}FeN_8P_2$	$C_{33}H_{31}F_{12}FeN_9O_4P_4$
fw	800.27	974.58	806.34	963.46
color/habit	yellow/fragment	red/block	red/fragment	red/plate
cryst dimens [mm^3]	0.17 × 0.31 × 0.36	0.08 × 0.17 × 0.38	0.08 × 0.13 × 0.27	0.14 × 0.17 × 0.30
cryst syst	triclinic	orthorhombic	orthorhombic	monoclinic
space group	$P\bar{1}$ (No. 2)	*Pbcn* (No. 60)	*Pbcn* (No. 60)	$P2_1/c$ (No. 14)
a [Å]	10.175(2)	7.9824(5)	8.3093(2)	8.4369(3)
b [Å]	18.176(4)	21.9479(8)	21.6677(7)	22.6147(8)
c [Å]	18.604(5)	23.6689(11)	16.8372(6)	20.3046(8)
α [deg]	88.663(10)	90	90	90
β [deg]	75.247(10)	90	90	90.900(2)
γ [deg]	75.812(10)	90	90	90
V [$Å^3$]	3222.9(13)	4146.7(4)	3031.43(16)	3873.6(2)
Z	4	4	4	4
T [K]	123	123	123	123
D_{calcd} [g cm^{-3}]	1.649	1.561	1.767	1.652
μ [mm^{-1}]	0.763	0.539	0.714	0.582
F(000)	1624	1992	1624	1952
θ range [deg]	1.13−25.41	1.72−25.41	1.88−25.38	2.75−25.35
index ranges (*h*, *k*, *l*)	±12, ±21, ±22	±9, −24 to −25, ±28	±10, ±26, ±20	±10, ±27, ±24
no. of reflns collected	57865	40081	93186	76048
no. of indep reflns/R_{int}	11744	3794	2783	7077
no. of obsd reflns [$I > 2\sigma(I)$]	10430	3480	2445	5265
no. of data/restraint/param	11744/70/878	3794/48/321	2783/0/227	7077/0/553
R1/wR2 [$I > 2\sigma(I)$]	0.0321/0.0742	0.0591/0.1365	0.0365/0.1376	0.0510/0.1193
R1/wR2 (all data)	0.0379/0.0775	0.0642/0.1390	0.0432/0.1466	0.0775/0.1317
GOF (on F^2)	1.038	1.187	1.274	1.031
largest diff peak/hole [e $Å^{-3}$]	0.512/−0.497	1.571/−0.535	0.836/−0.574	1.081/−0.414

established that the use of coordinating additives greatly increases the reactivity, with the most prominent examples being the second-generation ruthenium alkylidene metathesis catalysis and methyltrioxorhenium oxidation catalysts.[33−48] Insights into the electronic impact of axially coordinated ligands in bioinspired iron complexes together with predictable oxidation potentials can lead to target-oriented modifications of their reactivity.

Hence, we describe coordination exchange reactions of phosphines and pyridine derivatives with **1** and evaluate their influence on the system. Derived from Koopmans' theorem, density functional theory (DFT)-calculated molecular orbital (MO) energies are directly correlated to the oxidation potentials, as determined by cyclic voltammetry (CV) for five new complexes. We show that the bioinspired electronic modification of oxidation potentials of a defined Fe-NHC complex is predictable. A fundamental understanding of these implications is of utmost interest for target-oriented electronic tuning of iron(II) complexes and therefore for manipulating their reactivity toward future applications in catalysis or for fine-tuning of the existing catalytic systems.

EXPERIMENTAL SECTION

General Procedures. All chemicals were purchased from commercial suppliers and used without further purification. Anhydrous and oxygen-free acetonitrile was obtained from an MBraun solvent purification system, and analytical-grade acetone (99.9%) was degassed by the freeze−pump−thaw technique prior to its use as a solvent. Complex **1** was synthesized according to literature-known procedures.[31,49] Liquid NMR spectra were recorded on a Bruker Avance DPX 400, a Bruker Ultrashield 500 Plus with a cryo unit, and a Bruker Ultrashield 500. Chemical shifts are given in parts per million (ppm), and the spectra were referenced using the residual solvent shifts as internal standards (acetone-d_6; ^{1}H NMR, δ 2.05; ^{13}C NMR, δ 206.26). Electrospray ionization mass spectrometry (ESI-MS) analyses were performed on a Thermo Scientific LCQ/Fleet spectrometer by Thermo Fisher Scientific. A Jasco V-550 UV−vis spectrometer was used for collection of the UV−vis absorption spectra, and for every sample, 2 mg of the respective compound was dissolved in 8 mL of acetone. Elemental analysis was obtained from the microanalytical laboratory of TUM. Experimental procedures for reactions of the starting complex **1** with trimethylphosphine (PMe_3) to form disubstituted complex **2** and monosubstituted complex **2a**, as well as with triphenylphosphine (PPh_3), 4-(dimethylamino)pyridine (DMAP), pyridine (py), and methyl isonicotinate (Me^inico) to form complexes **3**−**6**, respectively, can be found in the Supporting Information (SI).

CV. A GAMRY Reference 600 potentiostat was used, together with eDAQ electrochemical reaction vessels (3.0 mL), for CV measurements. Platinum electrodes from eDAQ were chosen as the working and counter electrodes and Ag/AgCl (3.4 M in KCl) from eDAQ as the reference electrode. For all measurements, 3.0 mg of the respective compound was dissolved in 1.0 mL of degassed acetone, containing 0.1 mmol of tetrabutylammonium hexafluorophosphate. The potential was scanned with 100 mV s^{-1} from 0.0 to 1.5 V versus the Ag/AgCl redox couple, and the obtained values were referenced versus the Fc/Fc^+ redox couple as the internal standard (0.48 V vs SCE).[50]

Single-Crystal X-ray Diffraction. For crystallization of compounds **2**, **4**, and **6**, diethyl ether was allowed to diffuse slowly into an acetonitrile solution of **1** and excess of PMe_3, DMAP, or Me^inico, respectively. In the case of **5**, a saturated solution of the starting complex **1** in py was prepared, and again slow diffusion of diethyl ether into the solution resulted in the formation of a single crystalline material of **5**. Details on the collection of crystallographic data can be found in Table 1 as well as in the SI.

DFT Calculations. All calculations were performed with *Gaussian 09*[51] using the DFT/Hartree−Fock hybrid model Becke3LYP.[52,53] For

dx.doi.org/10.1021/ic501613a | *Inorg. Chem.* 2014, 53, 11573−11583

geometry optimizations, the split-valence double-ζ (DZ) basis set 6-31G(d)[54−56] was used for all atoms except iron, which was described with the SDD basis set as implemented in *Gaussian 09*, applying an effective core potential with a DZ description of the valence electrons.[57] This basis set combination is denoted as B1 in this Article. Solvation effects were taken into account by using the conductor-like polarizable continuum solvation model with acetonitrile as the solvent.[58,59] No symmetry or internal coordinate constraints were applied during optimization. All reported ground states were verified as being true minima by the absence of negative eigenvalues in vibrational frequency analysis. XYZ coordinates for all calculated compounds can be found in the SI. Single-point calculations on all optimized structures were performed to ensure energy convergence by using the triple-ζ basis set 6-311++G(d,p) on all atoms, denoted as B2.[60−64]

RESULTS AND DISCUSSION

Synthesis and Characterization. The starting complex **1**, bearing a rigid tetradentate NCCN ligand and two axial acetonitrile ligands, was synthesized according to previously reported procedures.[31,49] Both acetonitrile ligands are prone to ligand-exchange reactions, and PMe_3 and PPh_3, featuring different Tolman cone angles of 118° and 145°, respectively, were introduced as ligands in the axial positions.[65] The addition of excess PMe_3 to a solution of **1** in acetonitrile at room temperature gave complex **2** in 66% yield, while the reaction of PPh_3 and **1** in acetone at low temperature allowed isolation of complex **3** in 74% yield (Scheme 1).

Scheme 1. Reactions of Complex 1 with PMe_3, PPh_3, DMAP, py, and Me^{i}nico To Form Complexes 2−6, Respectively[a]

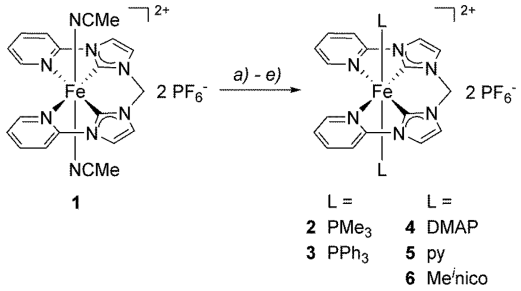

[a](a) Excess PMe_3, MeCN, room temperature. (b) Excess PPh_3, acetone, −78 °C to room temperature. (c) Excess DMAP, MeCN, room temperature. (d) Excess py, acetone, −78 °C to room temperature. (e) Excess Me^{i}nico, acetone, −78 °C to room temperature.

PMe_3, a strong σ donor, showed significantly stronger interaction with the iron center than acetonitrile; therefore, no exchange with MeCN was observed once the phosphine is coordinated to iron.[66] Also, only the disubstituted complex was formed, and a monosubstituted complex bearing one MeCN and one PMe_3 was not observed as the byproduct. However, the addition of PPh_3 to a solution of **1** in MeCN led to different results. Even in the presence of a large excess of PPh_3 (>30 equiv), a mixture of mono- and disubstituted products was always indicated by NMR spectroscopy. In contrast to PMe_3, PPh_3 not only has higher steric demand but also exhibits poorer σ-donor strength and is therefore in continuous exchange with acetonitrile solvent ligands.[65,66] Using acetone instead of MeCN as the solvent allowed complex **3** to form exclusively from **1** and excess PPh_3 (Scheme 1). Interestingly, in acetone the reactivity of **1** is increased significantly as a result of the poorer donor ability of acetone compared to acetonitrile. Consequently, all reactions in acetone have to be performed at low temperature (−78 °C) in order to avoid decomposition of **1**, which occurs slowly at room temperature even under inert conditions.

Comprehensive NMR spectroscopic data were collected, i.e., ^1H, ^{13}C, and ^{31}P NMR as well as $^1H-^1H$ COSY and $^1H-^{13}C$ HSQC (see the SI for all data). In ^1H NMR spectroscopy, a signal was observed for these and all of the following complexes that is shifted significantly downfield in the range of 9.50−10.50 ppm; it was assigned to the signal of the ortho protons of the pyridyl moieties of the symmetric tetradentate ligand. The relative shift of this signal changes remarkably with coordination of the axial substituents of different σ-donor strength, being 9.53 ppm in the case of PMe_3-substituted complex **2** and 10.17 ppm for PPh_3-substituted complex **3**. Low-temperature NMR experiments were required in order to obtain data of **1** for comparison because **1** decomposes in acetone at room temperature over time as mentioned before. ^1H NMR spectroscopy at −40 °C revealed a relative shift of 9.89 ppm for the ortho protons' signal. For complex **2**, single crystals suitable for X-ray diffraction were obtained, and the molecular structure is shown in Figure 2.

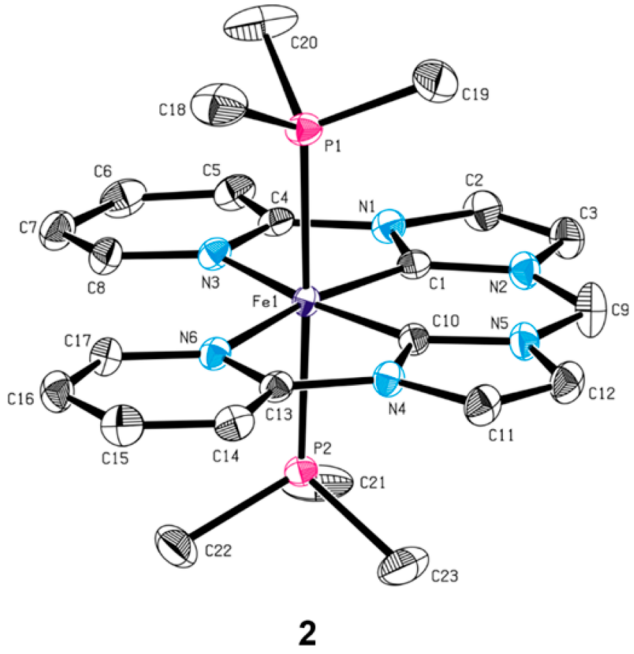

2

Figure 2. ORTEP representation of the dicationic fragment of complex **2**. Thermal ellipsoids are shown at the 50% probability level. Hydrogen atoms and PF_6^- anions are omitted for clarity. Selected bond lengths [Å] and angles [deg]: Fe1−C1 1.820(3), Fe1−C10 1.818(3), Fe1−N3 2.068(2), Fe1−N6 2.069(2), Fe1−P1 2.269(2), Fe1−P2 2.263(2); P1−Fe1−P2 177.42(3), N3−Fe1−N6 114.15(9).

Analogous to previously published X-ray data of **1**, complex **2** exhibits slightly distorted octahedral coordination geometry, with the tetradentate NCCN ligand coordinated in a square-planar fashion and the PMe_3 ligands coordinated trans to each other in axial positions. A more detailed presentation of the bond lengths in comparison to the other structures introduced in this Article can be found below, together with geometry parameters obtained from DFT calculations.

dx.doi.org/10.1021/ic501613a | *Inorg. Chem.* 2014, 53, 11573−11583

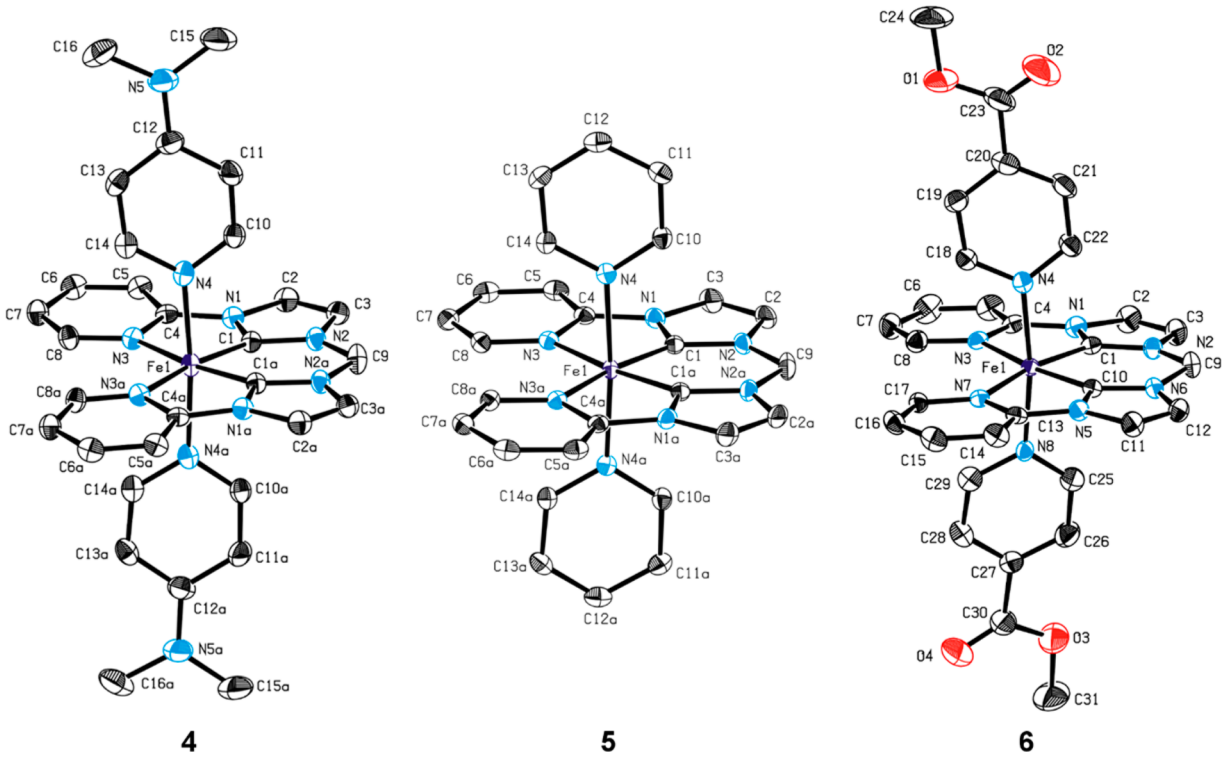

Figure 3. ORTEP representation of the dicationic fragments of complexes **4** (left), **5** (middle), and **6** (right) with thermal ellipsoids shown at the 50% probability level. Hydrogen atoms, PF_6^- anions, and cocrystallized solvent molecules are omitted for clarity. Selected bond lengths [Å] and angles [deg]: (**4**) Fe1−C1 1.819(3), Fe1−N3 2.084(3), Fe1−N4 2.014(3); N4−Fe1−N4a 174.35(15), N3−Fe1−N3a 113.49(15). Symmetry code: (a) $-x, y, -z + {}^3/_2$. (**5**) Fe1−C1 1.818(2), Fe1−N3 2.089(2), Fe1−N4 2.012(2); N4−Fe1−N4a 175.45(11), N3−Fe1−N3a 113.78(11). Symmetry code: (a) $-x + 2, y, -z + {}^3/_2$. (**6**) Fe1−C1 1.832(3), Fe1−C10 1.835(3), Fe1−N3 2.127(3), Fe1−N7 2.098(3), Fe1−N4 2.009(3), Fe1−N8 1.994(3); N4−Fe1−N8 171.46(11), N3−Fe1−N7 115.50(11).

Compound **1** was also treated with py and its donor- and acceptor-substituted derivatives DMAP and Me^{i}nico, leading to complexes **4**−**6**, which were obtained in yields of 70%, 79%, and 78%, respectively (Scheme 1). Analogous to the synthesis of **3**, it was also possible to isolate **4** when acetone was used as the solvent instead of acetonitrile. When the ligand was changed from the electron-rich DMAP to an unsubstituted py, only partial conversion was observed in MeCN and a mixture of mono- and disubstituted complexes can be obtained. As described for the synthesis of **3**, using acetone as the solvent for the ligand-exchange reaction with py led to clean conversion of **1** to **5**, giving the desired target compound as an orange powder in 79% yield. When the same methodology was applied to the synthesis of **6**, the disubstituted complex with Me^{i}nico as axial ligands was obtained as a red powder in 78% yield from the reaction of **1** with excess Me^{i}nico in acetone at low temperature.

Compounds **4**−**6** were characterized by NMR spectroscopy as well as by mass spectrometry and elemental analysis. In the ^{1}H NMR spectra, the signal of the ortho protons of the pyridyl moieties of the NCCN ligand appears as a doublet at 10.26 ppm for the DMAP-substituted complex **4**, at 10.34 ppm for the py-substituted complex **5**, and at 10.31 ppm for the Me^{i}nico-substituted complex **6**. Compounds **4**−**6** were further characterized by means of single-crystal X-ray structural analysis, and as in the case of **2**, the iron centers in **4**−**6** exhibit distorted octahedral geometry. A graphical representation of the molecular structures of **4**−**6** is given in Figure 3, together with selected bond lengths and angles; e.g., the bond length from the iron center to the axially coordinated nitrogen Fe1−N4 (and Fe1−N4a) is 2.014(3) Å in the case of **4**. For the py-substituted complex **5**, the Fe1−N4 (and Fe1−N4a) bond is 2.012(2) Å, whereas the molecular structure of **6** reveals a shorter Fe1−N4 bond length of 2.009(3) Å and a trans Fe1−N8 bond length of 1.994(3) Å. The molecular structure of **6** exhibits lower symmetry; therefore, two different bond lengths were observed for coordination of the axial ligands to the iron center.

For **4**−**6**, the trend toward slightly shorter Fe−N_{ax} bond lengths from DMAP via py to Me^{i}nico can be associated with the π-acceptor ability of the axial ligands, which is lowest for DMAP and highest for Me^{i}nico. A facilitated overlap of the d orbitals of the iron center with the π orbitals of the coordinating py's with better π-acceptor ability is feasible, resulting in a higher bond order in the case of better π-acceptor ligands. At the same time, the bond lengths from the equatorial pyridyl moieties to the iron center (Fe−N_{eq}) are elongated from **4** to **6**, indicating that the Fe−N_{eq} bond in the equatorial plane is weakened upon coordination of better π acceptors in the axial positions. The Fe−C_{NHC} bond was found to be remarkably short in all cases, ranging from 1.837(2) to 1.818(2) Å, while for other reported Fe^{II}-NHC complexes, the Fe−C_{NHC} bonds are typically longer, e.g., 1.979−2.052 Å for octahedral complexes with macrocyclic tetracarbene ligands or 2.177 Å for three-coordinate monocarbene-ligated iron complexes, albeit in a high-spin state.[25,67,68] For **1**−**6**, coordination of the pyridyl moieties of the tetradentate NCCN ligand causes the Fe−C_{NHC} bonds to shorten as a result of the rigid ligand structure. In the case of macrocyclic tetradentate ligands, no comparable rigidity

dx.doi.org/10.1021/ic501613a | Inorg. Chem. 2014, 53, 11573−11583

Table 2. Selected Bond Lengths [Å] and Angles [deg] of the First Coordination Sphere of 1, 2, and 4−6 As Determined by Single-Crystal X-ray Diffraction and Obtained from DFT Calculations on a B3LYP/B1 Level of Theory for 1−6[a]

			exchanged axial ligands				
		1 (MeCN)	2 (PMe_3)	3 (PPh_3)	4 (DMAP)	5 (py)	6 (Me^inico)
Fe−X_{ax} [Å]	X-ray	1.915(2)	2.269(2), 2.263(2)		2.014(3)	2.012(2)	2.009(3), 1.994(3)
	DFT	1.947	2.347	2.494	2.067	2.071	2.063
Fe−C_{NHC} [Å]	X-ray	1.837(2)	1.820(3), 1.818(3)		1.819(3)	1.818(2)	1.832(3), 1.835(3)
	DFT	1.867	1.851	1.870	1.858	1.864	1.868
Fe−N_{eq} [Å]	X-ray	2.096(2)	2.068(2), 2.069(2)		2.084(3)	2.089(2)	2.127(3), 2.098(3)
	DFT	2.162	2.156	2.221	2.205	2.207	2.217
X_{ax}−Fe−X_{ax} [deg]	X-ray	172.23(7)	177.42(3)		174.35(15)	175.45(11)	171.46(11)
	DFT	172.84	172.71	175.06	171.14	171.23	171.11

[a] X_{ax} corresponds to the coordinated donor atoms in axial positions, C_{NHC} represents the coordinated carbon atoms of the NHC units, and N_{eq} represents the nitrogen atoms of the pyridyl functionalities in the tetradentate NCCN ligand. X-ray data of **1** have been reported previously.[31]

is induced by the ligand scaffold, and therefore the Fe−C_{NHC} bonds are longer.

For all complexes, geometry optimizations based on the molecular structures as determined by X-ray diffraction were conducted on a B3LYP/B1 level of theory (see the Experimental Section) except for **3**, where no single crystals could be obtained. In general, DFT-obtained geometries were in good accordance with X-ray molecular structures. Also, the above-mentioned short Fe−C_{NHC} bond lengths are reflected by the DFT calculations, however to a smaller extent. An overview of the most relevant bond lengths and angles determined by X-ray diffraction as well as values obtained from DFT calculations is given in Table 2.

Electrochemical Investigations. In order to elucidate the electronic situation of disubstituted complexes **2**−**6**, all complexes were subjected to electrochemical oxidation utilizing CV. For **1**, the respective data have been reported earlier with a half-cell potential of $E_{1/2}$ = 423 mV for one-electron oxidation of Fe^{II} to Fe^{III}, and the process showed total reversibility.[31] With ligands of different donor ability replacing the axial acetonitrile ligands of **1**, a change of $E_{1/2}$ is expected for complexes **2**−**6**, and the experimentally gained cyclic voltammograms are shown in Figure 4.

In all five cases, one-electron oxidation in the range of 79−440 mV was found and assigned to the Fe^{II}/Fe^{III} oxidation, which is fully reversible for **2** and **4** and quasi-reversible for **3**, **5**, and **6**. Within each additive class (phosphines and py derivatives), a relationship between the π-back-bonding ability of the axial ligands and the oxidation potential is evident, with PPh_3 being a better π acceptor than PMe_3, and for the py derivatives, the π-acceptor ability increases from DMAP via py to Me^inico.[69] The half-cell potential of **2** (PMe_3-ligated) was determined as $E_{1/2}$ = 283 mV, whereas **3** (PPh_3-ligated) exhibits a significantly higher half-cell potential of $E_{1/2}$ = 440 mV. In the case of py and its derivatives, $E_{1/2}$ was found to be 79 mV in the case of **4** (DMAP-ligated) and 333 mV in the case of **5** (py-ligated), and the CV of **6** (Me^inico-ligated) revealed a half-cell potential of $E_{1/2}$ = 388 mV. Hence, the higher the π-back-bonding ability of the axial ligands, the higher the required potential for oxidation of the respective complexes. The CV results confirmed the expected change of the electrochemical behavior upon the introduction of ligands of different bonding abilities when compounds with the same class of axial ligands are compared. However, in order to understand the impact of coordinated axial ligands without being limited to one class of ligands for a detailed comparison, more information on energies on a MO level are required.

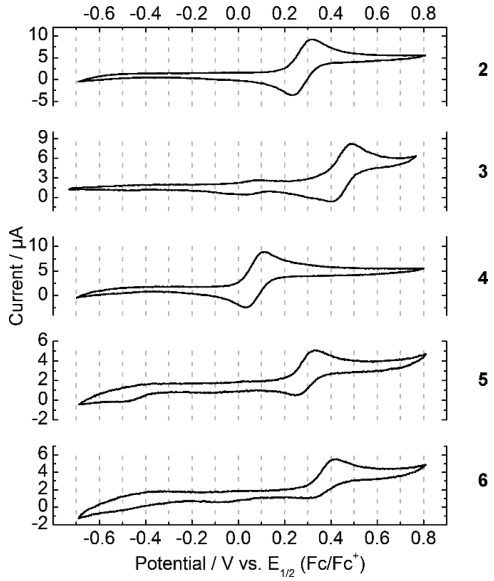

Figure 4. Cyclic voltammograms obtained for complexes **2**−**6**. For each experiment, 3 mg of the respective complex was dissolved in 1 mL of a 0.1 M solution of tetrabutylammonium hexafluorophosphate in acetone. The potential was scanned at 100 mV s^{-1} from 0.0 to 1.5 V versus Ag/AgCl, and the presented potential values were referenced to the Fc/Fc^+ redox couple as the internal standard (0.48 V vs SCE).[50] Half-cell potentials $E_{1/2}$ were identified as follows (vs Fc/Fc^+): 283 mV (**2**), 440 mV (**3**), 79 mV (**4**), 333 mV (**5**), and 388 mV (**6**).

Theoretical Considerations. Derived from Koopmans' theorem, which states that, in closed-shell Hartree−Fock theory, the ionization potential is equal to the negative highest occupied molecular orbital (HOMO) energy,[70] a DFT-based approach was used to investigate correlations between the HOMO energies of **2**−**6** and the experimentally determined oxidation potentials, as has been reported for other cases.[71] For all complexes, single-point calculations on the B3LYP/B2 level of theory (see the Experimental Section) were carried out on the previously described geometries obtained from geometry optimizations on the B3LYP/B1 level, and the resulting energies for HOMOs and lowest unoccupied molecular orbitals (LUMOs) are listed in Table 3 together with the CV oxidation potentials.

Compared to the starting complex **1**, E_{HOMO} is lowered and therefore better stabilized for **3** and **6**, both bearing axial ligands with the highest π-acceptor ability within their class of ligands used in this work. A higher E_{HOMO} compared to that of **1** was

dx.doi.org/10.1021/ic501613a | Inorg. Chem. 2014, 53, 11573−11583

Table 3. MO Energies of Complexes 1−6 As Calculated by DFT on the B3LYP/B2 Level of Theory Listed for the HOMO−1 (E_{HOMO-1}), HOMO (E_{HOMO}), and LUMO (E_{LUMO}) as Well as for the Gap between the HOMO and LUMO (ΔE_{Gap})[a]

	E_{HOMO-1} [eV]	E_{HOMO} [eV]	E_{LUMO} [eV]	ΔE_{Gap} [eV]	$E_{1/2}$ [mV]
1	−6.46	−6.30	−2.17	4.13	423[b]
2	−6.30	−6.11	−2.17	3.94	283
3	−6.47	−6.33	−2.24	4.09	440
4	−6.00	−5.76	−2.13	3.64	79
5	−6.24	−6.22	−2.22	4.00	333
6	−6.34	−6.34	−2.84	3.50	388

[a]Also, the half-cell potentials ($E_{1/2}$) determined experimentally by CV are given for all compounds. [b]Measured in MeCN.

calculated for **2**, **4**, and **5**, being the highest in the case of **4** with DMAP ligands in axial positions that are capable of π donation; hence, the HOMO is destabilized significantly. In the case of **6** and, to a smaller extent, also in the case of **5**, the two HOMOs are understood as degenerate orbitals, which stands in clear contrast to **1**−**4**. Notably, the energies of the respective LUMOs are not affected as significantly as the HOMOs, and yet the same trends were observed with the exception of complex **6**, which shows a LUMO with extensively lower energy. As a consequence of destabilization of the HOMO of **4** and stabilization of the LUMO of **6**, both complexes feature the lowest HOMO−LUMO gap (ΔE_{Gap}; compare Table 3). Still, with $\Delta E_{Gap} \geq 3.50$ eV for all complexes, the low-spin state of **1**−**6** is clearly illustrated.

A distinct correlation between the calculated E_{HOMO} and measured $E_{1/2}$ is evident because for both dimensions the same trends were observed regarding the π-acceptor ability of the axial ligands. Further data analysis revealed a linear relationship between E_{HOMO} and $E_{1/2}$ without limitations to the ligand class, and the linear fit with $R^2 = 0.995$ is shown in Figure 5.

The correlation between the HOMO energy and oxidation potential emphasizes the impact of electronic modification by the coordination of additives. As shown in Figure 5, the addition of DMAP to **1** results in a compound that is more prone to oxidation compared to the addition of PPh_3 or Me^{i}nico with up to 361 mV difference in the half-cell potential. By using the linear relationship between $E_{1/2}$ and E_{HOMO} ($E_{1/2} = -538E_{HOMO} - 3016$; see Figure 5), the oxidation potential of a hypothetical derivative of **1** with two axial PCy_3 ligands could be predicted. DFT calculations resulted in a value of $E_{HOMO} = -6.10$ eV in the case of two axial PCy_3 ligands; on the basis of the linear fit, the oxidation potential is predicted as $E_{1/2} = 268$ mV. These results are similar to the ones obtained for PMe_3 (**2**). Geometry data of the DFT-optimized structure of the PCy_3-ligated complex are given in the SI.

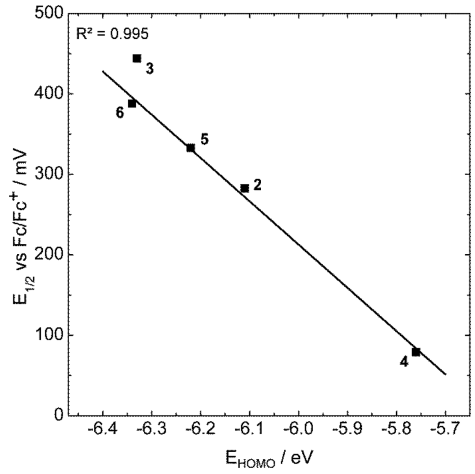

Figure 5. Linear relationship of the experimental half-cell potential $E_{1/2}$ versus Fc/Fc^+ as determined by CV and DFT-calculated energies of the HOMOs (E_{HOMO}) on the B3LYP/B2 level of theory for complexes **2**−**6**. The values of **3** were not included in the linear fit because **3** did not exhibit full reversibility for at least 10 cycles in the CV experiment. Linear equation: $E_{1/2} = -538E_{HOMO} - 3016$.

On the basis of the experimentally validated DFT data, a more thorough investigation of orbital geometries and energies was pursued in order to understand the differences between phosphine- and py-based ligands on a more fundamental level. Therefore, the HOMOs and LUMOs of **1**−**6** were visualized and the considered energies extended to all MOs from HOMO−4 to LUMO+4 (Figure 6).

Visualization of a HOMO often helps to evaluate the orbitals affected upon removal of an electron, and in the case of redox-active ligand systems, DFT-based approaches are employed for distinction between ligand- and metal-centered oxidation.[72−74] Also, the character of a d orbital that contributes to the respective MO can be described. It is evident from Figure 6 that for all complexes the iron center contributes to the corresponding HOMO, and with the exception of **4**, the same d orbital of iron is involved. Additionally, only minor differences between the HOMOs of **1**−**3**, **5**, and **6** were observed because for **1** and **3** only minor π-back-bonding to the axial ligand was revealed in the HOMOs and the majority of the respective HOMOs is located at the iron center and the coordinated NHC units. A different situation is given in the case of **4**, with contribution of the resonance structure of the axial DMAP ligands to the HOMO at the expense of inclusion of the NHC units. These findings are in accordance with the results described before because **4** is easier oxidized and exhibits a significantly destabilized HOMO compared to the other complexes. Notably, compounds **5** and **6** possess quasi-degenerate HOMOs with an energy difference of less than 0.02 eV, and in both cases, the contribution of the resonance structures of the axial ligands was found in their HOMO−1 (for visualization, see the SI). In contrast to the HOMOs, ligand-centered LUMOs were observed for all complexes, with major contribution of the equatorial pyridyl moieties of the tetradentate NCCN ligand with the exception of **6**, where the LUMO is located exclusively on the aromatic system of the axial Me^{i}nico ligands. Taking the energies of the LUMOs (E_{LUMO}) into account, a clear correlation between E_{LUMO} and the localization of the respective LUMO was found because **6** exhibits a LUMO with considerably lower energy compared to **1**−**5**. Therefore, the influence on the MOs by py-based axial ligands is reversed for the donor-substituted DMAP and the acceptor-substituted Me^{i}nico.

Apart from the dimensions of HOMOs and LUMOs, Figure 6 also depicts the energies of the five HOMOs (HOMO−4 to HOMO) and five LUMOs (LUMO to LUMO+4). Interestingly, exchange of MeCN ligands (**1**) to the strongly σ-donating PMe_3 ligands (**2**) did not result in a significant change of the MO splitting pattern, with only the energies being influenced. However, for **3**, a clear change of the splitting pattern was observed, and HOMO−4 and HOMO−3 were strongly destabilized, whereas especially LUMO+4 shows

dx.doi.org/10.1021/ic501613a | Inorg. Chem. 2014, 53, 11573−11583

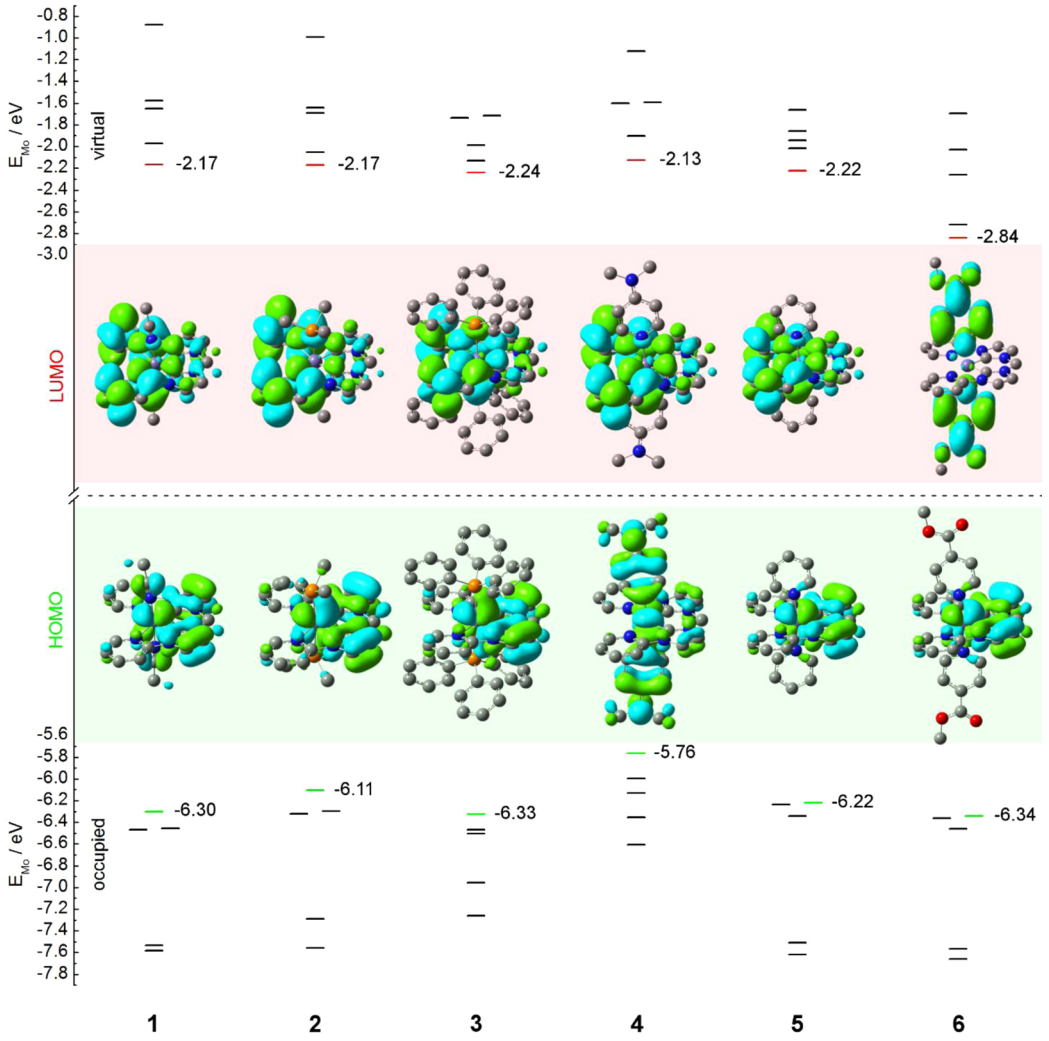

Figure 6. MO energies of HOMO−4 to LUMO+4 as predicted by DFT on the B3LYP/B2 level of theory and visualization of HOMOs (bottom) and LUMOs (top) for complexes **1**−**6** including exact values of E_{MO} for all HOMOs and LUMOs. Orbitals with a difference in energy of 0.02 eV or less are treated as quasi-degenerate. Exact energies obtained from DFT calculations for all orbitals depicted here are listed in the SI together with enlarged pictures of the visualized HOMOs and LUMOs.

remarkably better stabilization. As mentioned before, DMAP strongly increases the energies of the occupied MOs, even resulting in the disappearance of the gap between the three HOMOs that are derived from the Fe d orbitals and HOMO−3 and HOMO−4 in complex **4**. Nevertheless, the virtual, unoccupied MOs of **4** are almost unaffected, and only minor changes compared to **1** were seen. The occupied MOs of **5** and **6** are similar in their splitting pattern, and only minor energy differences were found. However, the aforementioned remarkable stabilization of the virtual orbitals of **6** also results in a different splitting pattern of these MOs.

Although only the HOMO and LUMO energies are of interest for prediction of the impact of coordinating additives on the redox behavior of transition-metal complexes, a more comprehensive insight into the energies of MOs as introduced above can help in the understanding of other electronic properties, e.g., excitation of molecules by absorption of light. Hence, UV−vis absorption spectra of **1**−**6** were recorded (see Figure 7).

Within the phosphine-ligated complexes **2** (ε_{413} = 10470 M^{-1} cm^{-1}) and **3** (ε_{410} = 7220 M^{-1} cm^{-1}), the PMe_3 derivative **2** has a higher extinction coefficient. Within the observed range, **3** revealed three absorption maxima (517, 410, and 355 nm), whereas two absorption bands were observed in the case of **2** (413 and 348 nm). Typically, intense colors with extinction coefficients on this order of magnitude are caused by charge-transfer processes rather than the alternative Laporte-forbidden d−d transitions.[75] Hence, the observed absorption bands in the region of visual light are understood as charge-transfer bands. For the phosphines, only minor influence on charge-transfer processes is indicated by UV−vis absorption spectroscopy with the exception of the additional absorption band of **3**. These findings are reflected in the splitting patterns of the MOs of **1**−**3**. Only minor energy differences of the occupied MOs are observed, and for **3**, also the energies of some of the virtual, unoccupied orbitals are lowered. A very different situation was observed in the case of the py-based ligands and the corresponding complexes **4** (ε_{350} = 13134 M^{-1} cm^{-1}), **5** (ε_{395} = 6326 M^{-1} cm^{-1}), and **6** (ε_{446} = 6059 M^{-1} cm^{-1}). Two absorption maxima were revealed for all three complexes, at wavelengths of 482 and 350 nm for **4**, 445 and 395 nm for **5**, and 446 and 345 nm for **6**. For DMAP-coordinated complex **4**, the absorption band at 482 nm shows a red-shifted shoulder and also **6** exhibits a red-shifted shoulder at the 446 nm

dx.doi.org/10.1021/ic501613a | Inorg. Chem. 2014, 53, 11573−11583

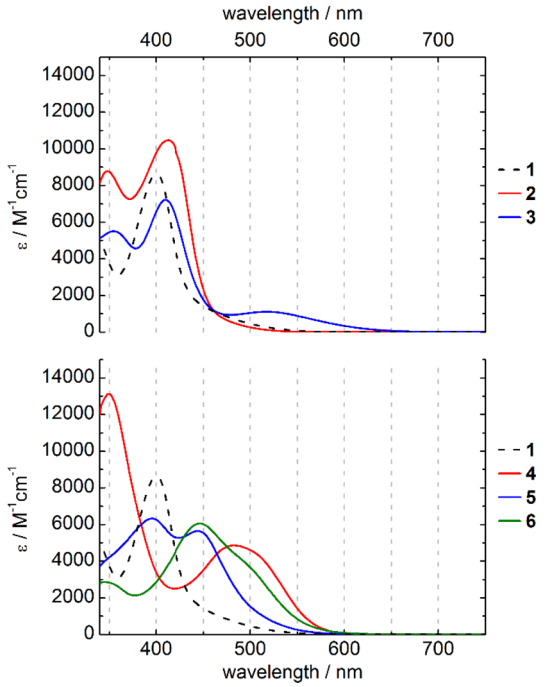

Figure 7. UV−vis absorption spectra of complexes **1**−**6**. Top: Starting complex **1** (dashed line) compared to phosphine derivatives **2** (red line) and **3** (blue line). Bottom: Absorption spectra of iron complexes bearing DMAP (**4**, red line), py (**5**, blue line), or Me^{i}nico (**6**, green line) ligands shown next to **1** (dashed line).

absorption band. Apparently, introducing differently substituted py ligands into the axial positions strongly influences the nature of electronic excitations and related charge-transfer bands. This observation could be correlated to the MO splitting patterns of **4**−**6** (Figure 6) because the energies of either the HOMOs (in the case of **4**) or LUMOs (in the case of **6**) differ significantly. For a full assignment of electronic transitions to the UV−vis data, time-dependent DFT (TD-DFT) is required;[76] however, a full TD-DFT study exceeds the scope of this work and is currently of interest in our group.

Outlook on the Reactivity in Solution. As mentioned above, all complexes apart from **2** did undergo ligand exchange with MeCN upon dissolution of the compounds in acetonitrile, resulting in a mixture of disubstituted complexes **3**−**6**, starting complex **1**, and monosubstituted derivatives **3a**−**6a**, bearing one acetonitrile ligand and one remaining coordinated additive in their axial positions (Figure 8).

Identification of the mixtures is possible by tracing the relative shift of the ^{1}H NMR signal of the ortho proton of the pyridyl moieties in the NCCN ligand, which is influenced significantly by the type of axial ligand. In the respective acetonitrile solutions of **2**−**6**, the ratio of disubstituted, monosubstituted, and bis(acetonitrile)-ligated complex **1** differs

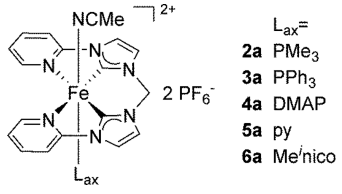

Figure 8. Structure of monosubstituted complexes **2a**−**6a**, bearing one acetonitrile and one coordinated additive L_{ax} in the axial positions.

significantly, depending on the axial ligand (see the SI for NMR data). As mentioned above, **2** did not undergo ligand exchange. In contrast, **3** releases exactly 1 equiv of PPh_3, which leads solely to **3a** (supported by ^{31}P NMR). The DMAP-substituted complex **4** results in a mixture of 65% **4** and 35% **4a** in an acetonitrile solution, whereas **5** gives a mixture of 6% **5**, 51% **5a**, and 43% **1**, and dissolving **6** in acetonitrile results in a mixture of 23% **6a** and 77% **1**. The presence of such monosubstituted complexes with one labile solvent ligand is of great interest because dissociation of such a placeholder ligand would lead to a five-coordinate, square-pyramidal iron center, exhibiting a free coordination site. On the basis of the theoretical investigations described above, the DFT approaches were transferred to the monosubstituted compounds **2a**−**6a**. Calculations of MO energies were performed, and the results for the five highest occupied and five lowest virtual MOs are shown in Figure 9 next to the data for **1**, together with visualizations of the HOMOs and LUMOs of all complexes.

Most interestingly, it is evident that only marginal differences between disubstituted complexes **2**−**6** and monosubstituted compounds **2a**−**6a** exist, concerning splitting patterns of the MOs as well as orbital energies. For most cases, the impact of additive coordination on MO energies was decreased, with only one additive coordinated to iron, and for PPh_3, no significant difference of the HOMO and LUMO energies between mono- and disubstituted complexes was calculated. Accordingly, the half-cell potentials of **2a**−**6a** could be predicted based on DFT-calculated E_{HOMO} from the linear relationship introduced before ($E_{1/2} = -538E_{HOMO} - 3016$; see Figure 5), and with the exception of DMAP-substituted compounds **4** and **4a**, the differences in the half-cell potentials between mono- and disubstituted complexes were small with 50 mV or less (Table 4).

Similar to the situation in **2**−**6**, the π-acceptor ability within each class of axial ligands was reflected by a clear trend in E_{HOMO} and $E_{1/2}$, respectively. Interestingly, the differences ($\Delta E_{1/2}$) between $E_{1/2,mono}$ and the half-cell potentials of disubstituted compounds **2**−**6** almost diminished for systems with better π-acceptor ligands in axial positions. For the phosphines, **2a** exhibits a half-cell potential of 47 mV higher compared to that of **2**, whereas $E_{1/2,mono}$ of **3a** is 50 mV lower than that of **3**. This observation was even clearer for the py-based axial ligands in the cases of **4a**−**6a**. DMAP-substituted **4a** required a 154 mV higher potential for oxidation; for py-substituted **5a**, the difference is only 19 mV, and similar to **3a**, with Me^{i}nico as a good π-acceptor ligand, the half-cell potential of **6a** was lowered by 9 mV compared to that of **6**. The consequences of partial axial ligand exchange in an acetonitrile solution could be estimated based on these results. In order to verify the theoretical predictions of half-cell potentials of the monosubstituted derivatives, attempts were undertaken to directly synthesize and isolate **2a**−**6a**. This was successful for **2a** with one PMe_3 ligand in the axial position (Scheme 2; see the SI for experimental details).

CV experiments with **2a** revealed a half-cell potential of 325 mV, which is in excellent accordance with the calculated value of 330 mV (Table 4; see the SI for the cyclic voltammogram of **2a**). This therefore validates the theoretical model that is used for prediction of the electrochemical properties. In addition to **2** and **2a**, it is evident from Table 4 that, with the exception of DMAP-substituted **4**, all compounds are interesting candidates for further investigations on the reactivity and applications in an acetonitrile solution. Their partial dissociation of one axial

dx.doi.org/10.1021/ic501613a | Inorg. Chem. 2014, 53, 11573−11583

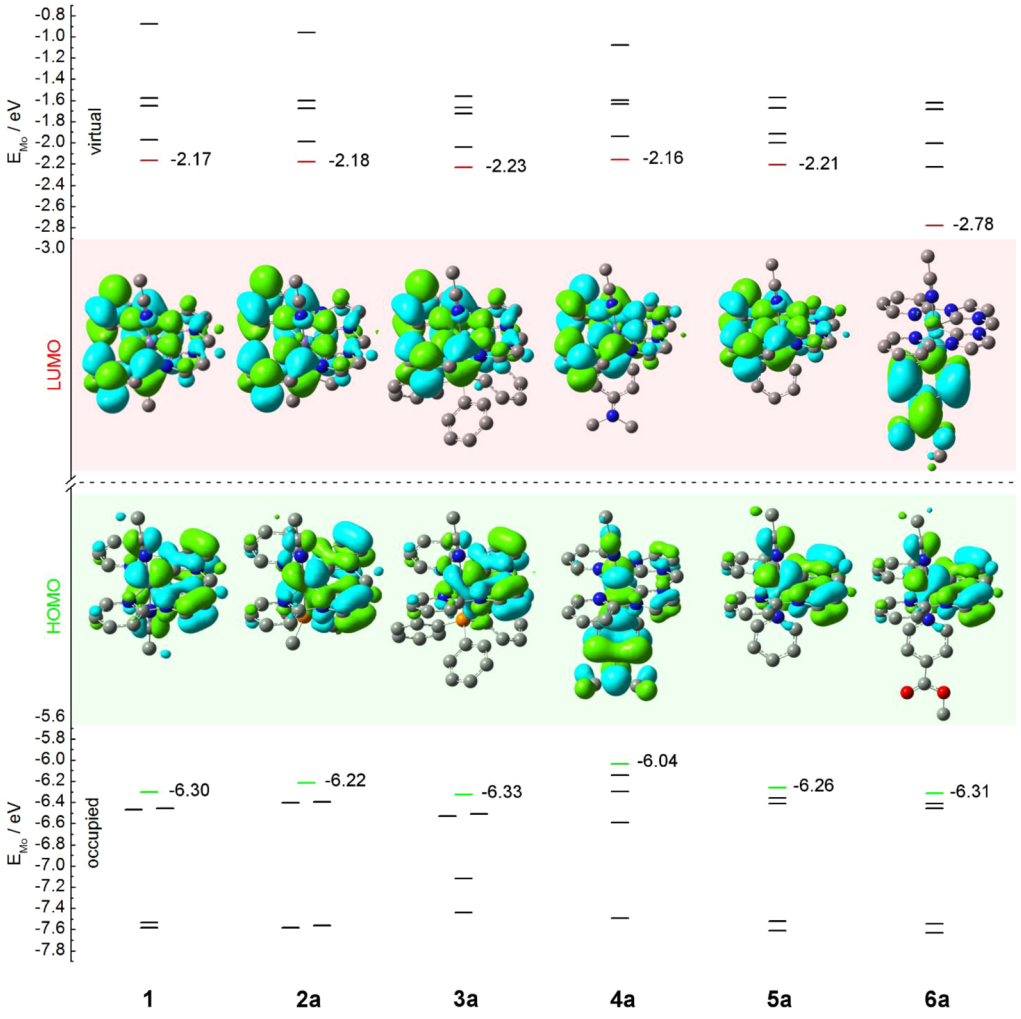

Figure 9. MO energies of HOMO−4 to LUMO+4 as predicted by DFT on the B3LYP/B2 level of theory and visualization of HOMOs (bottom) and LUMOs (top) for **1** and mono(additive)-substituted derivatives **2a**−**6a** of complexes **2**−**6**, including exact values of E_{MO} for all HOMOs and LUMOs. Orbitals with a difference in energy of 0.02 eV or less are treated as quasi-degenerate. Exact energies obtained from DFT calculations for all orbitals depicted here are listed in the SI together with enlarged pictures of the visualized HOMOs and LUMOs.

Table 4. MO Energies of Monosubstituted Complexes 2a−6a As Calculated by DFT on the B3LYP/B2 Level of Theory Shown for the HOMO (E_{HOMO}) and LUMO (E_{LUMO}) as Well as for the Gap between the HOMO and LUMO (ΔE_{Gap})[a]

	E_{HOMO} [eV]	E_{LUMO} [eV]	ΔE_{Gap} [eV]	$E_{1/2,mono}$ [mV]	$\Delta E_{1/2}$ [mV]
2a	−6.22	−2.18	4.04	330	47
3a	−6.33	−2.23	4.10	389	−50
4a	−6.04	−2.16	3.88	233	154
5a	−6.26	−2.21	4.05	352	19
6a	−6.31	−2.78	3.53	381	−9

[a]Also, the calculated half-cell potentials based on E_{HOMO} are shown ($E_{1/2,mono} = -538E_{HOMO} - 3016$), and the differences between $E_{1/2,mono}$ and the experimentally determined half-cell potentials of **2**−**6** are listed in the very right column ($\Delta E_{1/2}$).

ligand had almost no impact on the overall electronic situation based on MO energies.

CONCLUSIONS

The impact of a variety of axial ligands on the electronic properties of an octahedral Fe^{II}-NHC complex was investigated.

Scheme 2. Direct Synthesis of Monosubstituted Complex 2a with PMe_3 as the Axial Ligand

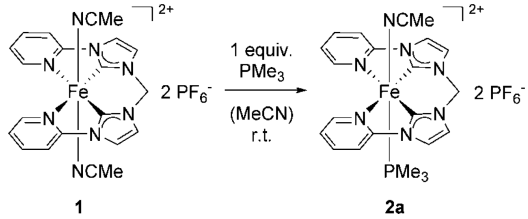

It could be shown that coordination of phosphines and py's in axial positions of the Fe-NHC complex results in defined complexes, which were characterized thoroughly prior to electronic investigations. From CV experiments, direct influences of coordinating additives on the potentials for Fe^{II}/Fe^{III} oxidation have been revealed and related to MO energies as determined by DFT calculations. Within the range of investigated axial ligands, DMAP features the highest impact on the half-cell potential, which is found to be 79 mV compared to 423 mV for the starting complex **1**. PPh_3 and Me^{i}nico, both being capable of π-back-bonding, influence the oxidation potential in the opposite direction, inducing a half-cell potential

dx.doi.org/10.1021/ic501613a | Inorg. Chem. 2014, 53, 11573−11583

of 440 and 388 mV, respectively. When Koopmans' theorem is adapted, a distinct linear correlation between the calculated E_{HOMO} and measured $E_{1/2}$ could be illustrated and, furthermore, a methodology for the quantitative prediction of the electronic properties induced by axial ligand exchange was established. A clear relation to the π-acceptor ability of the axially coordinated ligands has been revealed in terms of MO energies and splitting patterns. For instance, within the coordinating py derivatives, the energy of the HOMO of the iron complex is lowered from −5.76 eV for DMAP to −6.22 eV for py and to −6.34 eV for Me^{i}nico, which is the best π acceptor of all three ligands. The predictability of the electronic properties based on correlation of the experimental and theoretical approaches has been used for an outlook on the reactivity in solution, describing bioinspired systems with an apical ligand trans to an accessible coordination site in analogy to cyt-P450. It has been shown that the differences of predicted $E_{1/2}$ between monosubstituted complexes with one labile trans-coordinated solvent ligand and disubstituted complexes are lowered for π-acceptor ligands in the axial positions.

Overall, it is possible to provide fundamental insights into the effects of coordinating additives and to predict the resulting changes in the electronic properties. The described methodology will be useful for bioinspired electronic manipulation and thus for tuning the reactivity of artificial systems. Currently, the impact of these electronic changes of the Fe-NHC complex, induced by additive coordination, on the catalytic activity for a variety of transformations is under examination in our laboratories.

■ ASSOCIATED CONTENT

Ⓢ Supporting Information

Experimental procedures for the syntheses of **2**−**6**, listings of NMR data, details on DFT calculations (optimized structures, additional DFT-derived MO energies, and MO visualizations), an xyz file, and X-ray data in CIF format. This material is available free of charge via the Internet at http://pubs.acs.org. Crystallographic data for structures **2** and **4**−**6** have also been deposited with the Cambridge Crystallographic Data Centre (CCDC 992643−992646). These coordinates can be obtained, upon request, from the Director, Cambridge Crystallographic Data Centre, 12 Union Road, Cambridge CB2 1EZ, U.K.

■ AUTHOR INFORMATION

Corresponding Author

*E-mail: fritz.kuehn@ch.tum.de. Tel: +49 89 289 13096.

Notes

The authors declare no competing financial interest.

■ ACKNOWLEDGMENTS

This work is based on funding by Award KSA-C0069/UK-C0020, made by KAUST. The authors gratefully acknowledge the Gauss Centre for Supercomputing eV for funding this project by providing computing time on the GCS Supercomputer SuperMUC at Leibniz Supercomputing Centre, and the TUM-GS is acknowledged for support. J.W.K. thanks the Studienstiftung des Deutschen Volkes for support, and S.H. is thankful to Maike H. Wahl for her valuable contributions.

■ REFERENCES

(1) Que, L., Jr.; Tolman, W. B. *Nature* **2008**, *455*, 333−340.
(2) England, J.; Bigelow, J. O.; Van Heuvelen, K. M.; Farquhar, E. R.; Martinho, M.; Meier, K. K.; Frisch, J. R.; Munck, E.; Que, L. *Chem. Sci.* **2014**, *5*, 1204−1215.
(3) Ghosh, M.; Singh, K. K.; Panda, C.; Weitz, A.; Hendrich, M. P.; Collins, T. J.; Dhar, B. B.; Sen Gupta, S. *J. Am. Chem. Soc.* **2014**, *136*, 9524−9527.
(4) Widger, L. R.; Davies, C. G.; Yang, T.; Siegler, M. A.; Troeppner, O.; Jameson, G. N. L.; Ivanović-Burmazović, I.; Goldberg, D. P. *J. Am. Chem. Soc.* **2014**, *136*, 2699−2702.
(5) Wang, W.; Lippard, S. J. *J. Am. Chem. Soc.* **2014**, *136*, 2244−2247.
(6) Stoian, S. A.; Xue, G.; Bominaar, E. L.; Que, L.; Münck, E. *J. Am. Chem. Soc.* **2013**, *136*, 1545−1558.
(7) Cussó, O.; Garcia-Bosch, I.; Ribas, X.; Lloret-Fillol, J.; Costas, M. *J. Am. Chem. Soc.* **2013**, *135*, 14871−14878.
(8) McDonald, A. R.; Van Heuvelen, K. M.; Guo, Y.; Li, F.; Bominaar, E. L.; Münck, E.; Que, L. *Angew. Chem., Int. Ed.* **2012**, *51*, 9132−9136.
(9) Que, L. *Acc. Chem. Res.* **2007**, *40*, 493−500.
(10) Costas, M.; Mehn, M. P.; Jensen, M. P.; Que, L. *Chem. Rev.* **2004**, *104*, 939−986.
(11) Solomon, E. I.; Heppner, D. E.; Johnston, E. M.; Ginsbach, J. W.; Cirera, J.; Qayyum, M.; Kieber-Emmons, M. T.; Kjaergaard, C. H.; Hadt, R. G.; Tian, L. *Chem. Rev.* **2014**, *114*, 3659−3853.
(12) Talsi, E. P.; Bryliakov, K. P. *Coord. Chem. Rev.* **2012**, *256*, 1418−1434.
(13) Nam, W.; Ho, R.; Valentine, J. S. *J. Am. Chem. Soc.* **1991**, *113*, 7052−7054.
(14) Lubben, M.; Meetsma, A.; Wilkinson, E. C.; Feringa, B.; Que, L. *Angew. Chem., Int. Ed.* **1995**, *34*, 1512−1514.
(15) Britovsek, G. J. P.; England, J.; White, A. J. P. *Inorg. Chem.* **2005**, *44*, 8125−8134.
(16) England, J.; Davies, C. R.; Banaru, M.; White, A. J. P.; Britovsek, G. J. P. *Adv. Synth. Catal.* **2008**, *350*, 883−897.
(17) Mikhalyova, E. A.; Makhlynets, O. V.; Palluccio, T. D.; Filatov, A. S.; Rybak-Akimova, E. V. *Chem. Commun.* **2012**, *48*, 687−689.
(18) Comba, P.; Lee, Y.-M.; Nam, W.; Waleska, A. *Chem. Commun.* **2014**, *50*, 412−414.
(19) Li, Y.-Y.; Yu, S.; Wu, X.; Xiao, J.; Shen, W.-Y.; Dong, Z.-R.; Gao, J.-X. *J. Am. Chem. Soc.* **2014**, *136*, 4031−4039.
(20) Gopalaiah, K. *Chem. Rev.* **2013**, *113*, 3248−3296.
(21) Enthaler, S.; Junge, K.; Beller, M. *Angew. Chem., Int. Ed.* **2008**, *47*, 3317−3321.
(22) Nam, W. *Acc. Chem. Res.* **2007**, *40*, 522−531.
(23) Riener, K.; Haslinger, S.; Raba, A.; Högerl, M. P.; Cokoja, M.; Herrmann, W. A.; Kühn, F. E. *Chem. Rev.* **2014**, *114*, 5215−5272.
(24) Rohde, J.-U.; In, J.-H.; Lim, M. H.; Brennessel, W. W.; Bukowski, M. R.; Stubna, A.; Münck, E.; Nam, W.; Que, L. *Science* **2003**, *299*, 1037−1039.
(25) Meyer, S.; Klawitter, I.; Demeshko, S.; Bill, E.; Meyer, F. *Angew. Chem., Int. Ed.* **2013**, *52*, 901−905.
(26) Park, J.; Lee, Y.-M.; Nam, W.; Fukuzumi, S. *J. Am. Chem. Soc.* **2013**, *135*, 5052−5061.
(27) Shaik, S.; Cohen, S.; Wang, Y.; Chen, H.; Kumar, D.; Thiel, W. *Chem. Rev.* **2009**, *110*, 949−1017.
(28) Meunier, B.; de Visser, S. P.; Shaik, S. *Chem. Rev.* **2004**, *104*, 3947−3980.
(29) Li, F.; England, J.; Que, L. *J. Am. Chem. Soc.* **2010**, *132*, 2134−2135.
(30) Liu, L. V.; Hong, S.; Cho, J.; Nam, W.; Solomon, E. I. *J. Am. Chem. Soc.* **2013**, *135*, 3286−3299.
(31) Raba, A.; Cokoja, M.; Ewald, S.; Riener, K.; Herdtweck, E.; Pöthig, A.; Herrmann, W. A.; Kühn, F. E. *Organometallics* **2012**, *31*, 2793−2800.
(32) (a) Kück, J. W.; Raba, A.; Markovits, I. I. E.; Cokoja, M.; Kühn, F. E. *ChemCatChem* **2014**, *6*, 1882−1886. (b) Raba, A.; Cokoja, M.; Herrmann, W. A.; Kühn, F. E. *Chem. Commun.* **2014**, *50*, 11454−11457.
(33) Vougioukalakis, G. C.; Grubbs, R. H. *Chem. Rev.* **2009**, *110*, 1746−1787.

(34) Love, J. A.; Morgan, J. P.; Trnka, T. M.; Grubbs, R. H. *Angew. Chem., Int. Ed.* **2002**, *41*, 4035−4037.
(35) Huang, J.; Stevens, E. D.; Nolan, S. P.; Petersen, J. L. *J. Am. Chem. Soc.* **1999**, *121*, 2674−2678.
(36) Ackermann, L.; Fürstner, A.; Weskamp, T.; Kohl, F. J.; Herrmann, W. A. *Tetrahedron Lett.* **1999**, *40*, 4787−4790.
(37) Scholl, M.; Trnka, T. M.; Morgan, J. P.; Grubbs, R. H. *Tetrahedron Lett.* **1999**, *40*, 2247−2250.
(38) Copéret, C.; Adolfsson, H.; Sharpless, K. B. *Chem. Commun.* **1997**, *16*, 1565−1566.
(39) Herrmann, W. A.; Ding, H.; Kratzer, R. M.; Kühn, F. E.; Haider, J. J.; Fischer, R. W. *J. Organomet. Chem.* **1997**, *549*, 319−322.
(40) Rudolph, J.; Reddy, K. L.; Chiang, J. P.; Sharpless, K. B. *J. Am. Chem. Soc.* **1997**, *119*, 6189−6190.
(41) Herrmann, W. A.; Kratzer, R. M.; Ding, H.; Thiel, W. R.; Glas, H. *J. Organomet. Chem.* **1998**, *555*, 293−295.
(42) Wang, W.-D.; Espenson, J. H. *J. Am. Chem. Soc.* **1998**, *120*, 11335−11341.
(43) Adolfsson, H.; Converso, A.; Sharpless, K. B. *Tetrahedron Lett.* **1999**, *40*, 3991−3994.
(44) Kühn, F. E.; Santos, A. M.; Roesky, P. W.; Herdtweck, E.; Scherer, W.; Gisdakis, P.; Yudanov, I. V.; Di Valentin, C.; Rösch, N. *Chem.—Eur. J.* **1999**, *5*, 3603−3615.
(45) Altmann, P.; Kühn, F. E. *J. Organomet. Chem.* **2009**, *694*, 4032−4035.
(46) Zhou, M.-D.; Jain, K. R.; Günyar, A.; Baxter, P. N. W.; Herdtweck, E.; Kühn, F. E. *Eur. J. Inorg. Chem.* **2009**, *2009*, 2907−2914.
(47) Carril, M.; Altmann, P.; Drees, M.; Bonrath, W.; Netscher, T.; Schütz, J.; Kühn, F. E. *J. Catal.* **2011**, *283*, 55−67.
(48) Altmann, P.; Cokoja, M.; Kühn, F. E. *Eur. J. Inorg. Chem.* **2012**, *2012*, 3235−3239.
(49) Raba, A.; Anneser, M. R.; Jantke, D.; Cokoja, M.; Herrmann, W. A.; Kühn, F. E. *Tetrahedron Lett.* **2013**, *54*, 3384−3387.
(50) Connelly, N. G.; Geiger, W. E. *Chem. Rev.* **1996**, *96*, 877−910.
(51) Frisch, M. J.; Trucks, G. W.; Schlegel, H. B.; Scuseria, G. E.; Robb, M. A.; Cheeseman, J. R.; Scalmani, G.; Barone, V.; Mennucci, B.; Petersson, G. A.; Nakatsuji, H.; Caricato, M.; Li, X.; Hratchian, H. P.; Izmaylov, A. F.; Bloino, J.; Zheng, G.; Sonnenberg, J. L.; Hada, M.; Ehara, M.; Toyota, K.; Fukuda, R.; Hasegawa, J.; Ishida, M.; Nakajima, T.; Honda, Y.; Kitao, O.; Nakai, H.; Vreven, T.; Montgomery, J. A., Jr.; Peralta, J. E.; Ogliaro, F.; Bearpark, M.; Heyd, J. J.; Brothers, E.; Kudin, K. N.; Staroverov, V. N.; Kobayashi, R.; Normand, J.; Raghavachari, K.; Rendell, A.; Burant, J. C.; Iyengar, S. S.; Tomasi, J.; Cossi, M.; Rega, N.; Millam, J. M.; Klene, M.; Knox, J. E.; Cross, J. B.; Bakken, V.; Adamo, C.; Jaramillo, J.; Gomperts, R.; Stratmann, R. E.; Yazyev, O.; Austin, A. J.; Cammi, R.; Pomelli, C.; Ochterski, J. W.; Martin, R. L.; Morokuma, K.; Zakrzewski, V. G.; Voth, G. A.; Salvador, P.; Dannenberg, J. J.; Dapprich, S.; Daniels, A. D.; Farkas, Ö.; Foresman, J. B.; Ortiz, J. V.; Cioslowski, J.; Fox, D. J. *Gaussian 09*, revision D.01; Gaussian, Inc.: Wallingford, CT, 2009.
(52) Lee, C.; Yang, W.; Parr, R. G. *Phys. Rev. B: Condens. Matter Mater. Phys.* **1988**, *37*, 785−789.
(53) Becke, A. D. *J. Chem. Phys.* **1993**, *98*, 5648−5652.
(54) Ditchfield, R.; Hehre, W. J.; Pople, J. A. *J. Chem. Phys.* **1971**, *54*, 724−728.
(55) Hehre, W. J.; Ditchfield, R.; Pople, J. A. *J. Chem. Phys.* **1972**, *56*, 2257−2261.
(56) Francl, M. M.; Pietro, W. J.; Hehre, W. J.; Binkley, J. S.; Gordon, M. S.; DeFrees, D. J.; Pople, J. A. *J. Chem. Phys.* **1982**, *77*, 3654−3665.
(57) Dolg, M.; Wedig, U.; Stoll, H.; Preuss, H. *J. Chem. Phys.* **1987**, *86*, 866−872.
(58) Barone, V.; Cossi, M. *J. Phys. Chem. A* **1998**, *102*, 1995−2001.
(59) Cossi, M.; Rega, N.; Scalmani, G.; Barone, V. *J. Comput. Chem.* **2003**, *24*, 669−681.
(60) Wachters, A. J. H. *J. Chem. Phys.* **1970**, *52*, 1033−1036.
(61) Hay, P. J. *J. Chem. Phys.* **1977**, *66*, 4377−4384.
(62) Krishnan, R.; Binkley, J. S.; Seeger, R.; Pople, J. A. *J. Chem. Phys.* **1980**, *72*, 650−654.
(63) McLean, A. D.; Chandler, G. S. *J. Chem. Phys.* **1980**, *72*, 5639−5648.
(64) Raghavachari, K.; Trucks, G. W. *J. Chem. Phys.* **1989**, *91*, 1062−1065.
(65) Tolman, C. A. *Chem. Rev.* **1977**, *77*, 313−348.
(66) Haav, K.; Saame, J.; Kütt, A.; Leito, I. *Eur. J. Org. Chem.* **2012**, *2012*, 2167−2172.
(67) Danopoulos, A. A.; Braunstein, P.; Wesolek, M.; Monakhov, K. Y.; Rabu, P.; Robert, V. *Organometallics* **2012**, *31*, 4102−4105.
(68) Cramer, S. A.; Jenkins, D. M. *J. Am. Chem. Soc.* **2011**, *133*, 19342−19345.
(69) Crabtree, R. H. *The Organometallic Chemistry of the Transition Metals*; Wiley: New York, 2005.
(70) Koopmans, T. *Physica* **1934**, *1*, 104−113.
(71) Landman, M.; Pretorius, R.; Buitendach, B. E.; van Rooyen, P. H.; Conradie, J. *Organometallics* **2013**, *32*, 5491−5503.
(72) Blusch, L. K.; Craigo, K. E.; Martin-Diaconescu, V.; McQuarters, A. B.; Bill, E.; Dechert, S.; DeBeer, S.; Lehnert, N.; Meyer, F. *J. Am. Chem. Soc.* **2013**, *135*, 13892−13899.
(73) Nemykin, V. N.; Purchel, A. A.; Spaeth, A. D.; Barybin, M. V. *Inorg. Chem.* **2013**, *52*, 11004−11012.
(74) Das, S.; Karmakar, S.; Saha, D.; Baitalik, S. *Inorg. Chem.* **2013**, *52*, 6860−6879.
(75) Atkins, P. W.; Overton, T.; Rourke, J.; Weller, M.; Armstrong, F. *Shriver & Atkins' Inorganic Chemistry*, 5th ed.; Oxford University Press: Oxford, U.K., 2009.
(76) Akimov, A. V.; Neukirch, A. J.; Prezhdo, O. V. *Chem. Rev.* **2013**, *113*, 4496−4565.